

Direct numerical simulation of boundary layer transition in streamwise corner-flow

Oliver Schmidt, Björn Selent & Ulrich Rist

Institute of Aerodynamics and Gas Dynamics, University of Stuttgart, Germany

Abstract The process of laminar-turbulent transition in streamwise corner-flow is considered by means of direct numerical simulation (DNS). It is shown that transition triggered by harmonic forcing originates from the near-corner region in the shape of a turbulent wedge. The resulting mean flow deformation takes the shape of an outward bulge, and can be linked to experimental observations. A spectral analysis of the transient flow data is undertaken to elaborate on non-linear interactions, modal structures and spectral energy distribution. Additionally, the massive parallel performance of the DNS code on the Cray XE6 supercomputer is discussed and compared with the performance on previous vector architectures.

0.1 Introduction

The basic corner-flow setup consists of two semi-infinite perpendicular flat plates with the freestream parallel to the intersection axis as sketched in figure 0.1. It serves as a generic model for a variety of technical flows. Because of its practical relevance the corner-flow problem has been studied both, numerically and experimentally for more than 60 years starting with the early theoretical considerations by Carrier [3]. The reader is referred to the work of Zamir [17] for a comprehensive review of experimental work that was mainly conducted during that period. Until now, numerical studies were almost exclusively restricted to eigenvalue-based linear stability studies of the two-dimensional self-similar corner-flow solutions first obtained by Rubin and Grossman [14] and [8] for incompressible and general compressible flows, respectively. Overviews of the numerous numerical studies can be found, e.g. in the work of Galionis and Hall [5]. There exists a remarkable discrepancy between experiment and theory that has not been resolved. In linear stability studies, a critical

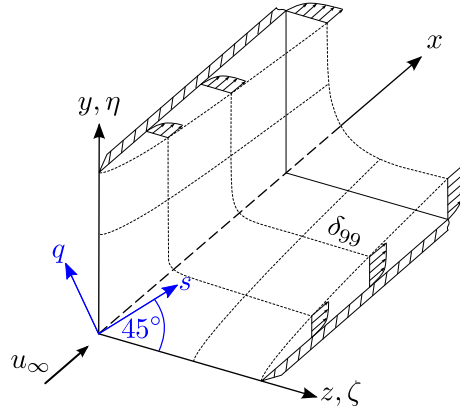


Fig. 0.1 Sketch of the flow in a streamwise corner: (x, y, z) denote the Cartesian coordinates with the x -coordinate in the streamwise direction, (η, ζ) the self-similar spanwise coordinates and (s, q) an auxiliary coordinate frame with the ordinate along the corner bisector. [16]

Reynolds number comparable to the one found for the closely related flat-plate scenario is found while rapid transition to turbulence at short distances after the leading edge is consistently observed in experiment. In the work at hand, we present the first direct numerical simulation of the transition process in axial corner-flow. The study is organized as follows: an introduction to the corner-flow problem is given in §0.1, the numerical setup and the laminar self-similar base state are discussed in §0.2, and the results are summarized in §0.3. The parallel performance of the direct numerical simulation code is addressed in §0.4. Final conclusions are given in §0.5.

0.2 Numerical setup and base state

Governing equations The flow of a compressible fluid is governed by the full Navier-Stokes equations

$$\frac{\partial \rho}{\partial t} = -\nabla \cdot \rho \mathbf{u}, \quad (0.1)$$

$$\frac{\partial \rho \mathbf{u}}{\partial t} = -\frac{1}{2} \nabla \cdot (\mathbf{u} \otimes \rho \mathbf{u} + \rho \mathbf{u} \otimes \mathbf{u}) - \nabla p + \frac{1}{\text{Re}} \nabla \cdot \boldsymbol{\tau}, \quad (0.2)$$

$$\frac{\partial \rho e}{\partial t} = -\nabla \cdot \rho e \mathbf{u} + \frac{1}{(\gamma - 1) \text{Re} \text{Pr} \text{Ma}_\infty^2} \nabla \cdot k \nabla T - \nabla \cdot \rho \mathbf{u} + \frac{1}{\text{Re}} \nabla \cdot \boldsymbol{\tau}, \quad (0.3)$$

where ρ is the density, $\mathbf{u} = (u, v, w)^T$ the vector of Cartesian velocity components, p the pressure, e the total energy, T the temperature and t the time. The dynamic viscosity μ and the thermal conductivity k are fluid properties and $\boldsymbol{\tau} = \mu (\nabla \mathbf{u} + \nabla \mathbf{u}^T) - \frac{2}{3} \mu (\nabla \cdot \mathbf{u}) \mathbf{I}$ the viscous stress tensor. All flow quantities are non-dimensionalized by their respective dimensional free-stream values denoted by $(\cdot)_\infty^*$ and the coordinates by the boundary layer displacement thickness δ_1^* . The dimensionless Reynolds number $\text{Re} = \rho_\infty^* u_\infty^* \delta_1^* / \mu_\infty^*$, Prandtl number $\text{Pr} = c_p^* \mu_\infty^* / k_\infty^*$, and

Mach number $Ma = u_\infty^*/a_\infty^*$ hence fully describe the flow. The set of governing equations 0.1 is closed by the ideal gas law $p = \rho T / (\gamma Ma_\infty^2)$ and Sutherland's law $\mu^*(T) = \mu_{ref}^* T^{3/2} (1 + T_s) / (T + T_s)$ that empirically relates viscosity and temperature. The empirical constants are given as $\mu_{ref}^* (T_{ref}^* = 280 \text{ K}) = 1.735 \times 10^{-5} \text{ kg/ms}$ and $T_s = 110.4 \text{ K} / T_\infty^*$. A technically relevant flow case with $Ma = 0.8$ and dry air at standard conditions is chosen for the study at hand. The corresponding Prandtl number, heat capacity ratio, and dimensional freestream properties are listed in table 0.1.

| Pr [-] | γ [-] | p_∞^* [hPa] | T_∞^* [K] | c_p [$\frac{\text{J}}{\text{kgK}}$] | R^* [$\frac{\text{J}}{\text{kgK}}$] |
|--------|--------------|--------------------|------------------|---|---|
| 0.714 | 1.4 | 1013.25 | 293.15 | 1005 | 287 |

Table 0.1 Dimensionless quantities and freestream properties.

Discretization Direct numerical simulation of transitional flows demands for accurate resolution of smallest flow structures, both spatially and temporal. In this work we use the designated DNS code *NS3D* [2, 1] with 6th-order accurate biased compact differences

$$\begin{aligned} \frac{1}{5} \frac{\partial q}{\partial \xi} \Big|_{j-1,+} + \frac{3}{5} \frac{\partial q}{\partial \xi} \Big|_{j,+} + \frac{1}{5} \frac{\partial q}{\partial \xi} \Big|_{j+1,+} &= \frac{-q_{j-2} - 19q_{j-1} + 11q_j + 9q_{j+1}}{30\Delta\xi}, \\ \frac{1}{5} \frac{\partial q}{\partial \xi} \Big|_{j-1,-} + \frac{3}{5} \frac{\partial q}{\partial \xi} \Big|_{j,-} + \frac{1}{5} \frac{\partial q}{\partial \xi} \Big|_{j+1,-} &= \frac{-9q_{j-1} - 11q_j + 19q_{j+1} + q_{j+2}}{30\Delta\xi}, \end{aligned} \quad (0.4)$$

used for the convective terms. The subscripts '+' and '-' denote up- and downwind biasing and j the grid point index in some direction ξ , respectively. First derivatives of viscous terms are computed using a standard symmetric compact finite difference stencil

$$\frac{\partial q}{\partial \xi} \Big|_{j-1} + 3 \frac{\partial q}{\partial \xi} \Big|_j + \frac{\partial q}{\partial \xi} \Big|_{j+1} = \frac{-q_{j-2} - 28q_{j-1} + 28q_{j+1} + q_{j+2}}{12\Delta\xi}. \quad (0.5)$$

Similarly, second derivatives are obtained directly as

$$2 \frac{\partial^2 q}{\partial \xi^2} \Big|_{j-1} + 11 \frac{\partial^2 q}{\partial \xi^2} \Big|_j + 2 \frac{\partial^2 q}{\partial \xi^2} \Big|_{j+1} = \frac{3q_{j-2} + 48q_{j-1} - 102q_j + 48q_{j+1} + 3q_{j+2}}{4\Delta\xi^2}. \quad (0.6)$$

A standard explicit 4th-order Runge-Kutta method is used for the temporal integration.

Base state and computational domain A fully three-dimensional simulation of the transitional flow field is not feasible because of the complex asymptotic behavior of the secondary cross flow, and pressure field. We hence rely on a perturbation formulation that allows us to calculate the perturbation flow field solely upon a

fixed steady base state. In the following, perturbation quantities are denoted by $(\cdot)'$ and the base state by $(\cdot)_0$. The implementation of the perturbation formulation is described in detail in [1]. The steady self-similar base state is calculated as a solution to the parabolized Navier-Stokes equation as in [16]. The base flow is depicted in figure 0.2. The complex nature of the secondary cross-flow becomes apparent in

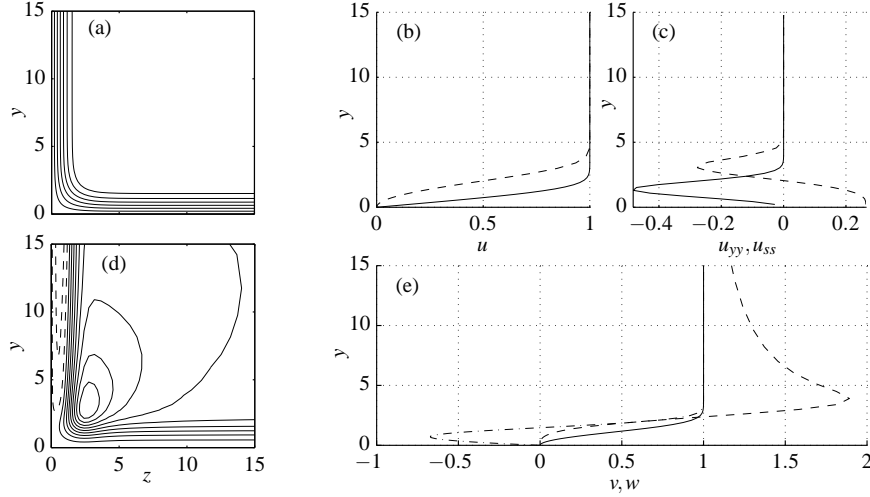


Fig. 0.2 Self-similar base flow; (a) isolines of the streamwise velocity $u(y,z)$; (b) streamwise velocity profiles: (—) far-field, $u(y,z \rightarrow \infty)$; (---) along the corner bisector, $u(y=z)$; (c) second partial derivatives of streamwise velocity profiles: (—) far-field, $u_{yy}(y,z \rightarrow \infty)$; (---) along the corner bisector, $u_{ss}(y=z)$; (d) isolines of the cross-flow velocity $v(y,z)$: (---) negative; (—) positive; (e) cross-flow velocity far-field profiles: (—) wall normal direction, $v(y,z \rightarrow \infty)$; (---) tangential direction, $w(y,z \rightarrow \infty)$; (-·-) along the corner bisector, $v(y=z) = w(y=z)$.

figure 0.2d. Also note that the streamwise velocity component becomes inflectional in the near-corner-region as indicated by the change of sign of the second derivative along the corner bisector coordinate s in 0.2c. Inflectional profiles are known to be inviscidly unstable.

| x_0 | Re_0 | x_1 | Re_1 | $x_{p,0}$ | $x_{p,1}$ | y_1, z_1 | N_x | N_y, N_z | Δt |
|--------|--------|--------|---------|-----------|-----------|------------|-------|------------|------------|
| 195.68 | 766.56 | 554.71 | 1290.31 | 197.12 | 208.61 | 54 | 1250 | 400 | 0.005 |
| 267.49 | | 396.74 | | | | 22.82 | 225 | 100 | |

Table 0.2 Computational domain for the direct numerical simulation; subscript (0) and (1) denote start and end, $N_{x,y,z}$ the number of grid points in the respective direction, $x_{p,0}$ and $x_{p,1}$ delimit the streamwise perturbation strip. The heating strip extent corresponds to 30 grid cells, starting at the 15th grid point. Blue numbers in the bottom line refer to the DMD subdomain depicted in figure 0.3b.

The extent and spatial resolution of the computational domain for the DNS and a smaller subdomain used for post-processing are summarized in table 0.2. The streamwise domain extent corresponds to a Reynolds number regime of $15 \times 10^4 \leq \text{Re}_x \leq 42.5 \times 10^4$ based on the distance from the leading edge. Simulations at lower, i.e. subcritical, Reynolds numbers are desirable but much more computationally demanding due to the fast boundary layer growth in that region and the associated necessity for a larger computational domain.

Boundary conditions Adiabatic no-slip wall boundary conditions are enforced on both walls. The wall pressure is extrapolated from the interior field and the density is calculated from the ideal gas law. Homogeneous Neumann conditions are applied on the inlet and on the far-field boundaries. On the outlet, a subsonic outflow condition [1] is applied. A sponge region is used at the inlet and outlet regions of the computational domain to cancel the fluctuations before reaching the boundaries in order to prevent reflection back into the solution domain. The sponge zone is restricted to the the outmost 2.5% of the inlet and outlet regions and follows a fifth-order polynomial distribution $\sigma(\xi) = \pm\sigma_{max}(1 - 6\xi^5 + 15\xi^4 - 10\xi^3)$ for $\xi \in [0, 1]$, where ξ is the locally scaled distance from the inlet and outlet boundary, respectively, and σ_{max} is the sponge amplitude or gain. A wall heating strip is used to force a harmonic perturbation along the walls. For this purpose, the adiabatic wall boundary condition is locally replaced within some streamwise extend $x_{p,0} \leq x \leq x_{p,1}$. A dipole distribution of the form

$$T' = a \frac{81}{16} (2\xi)^3 [3(2\xi)^2 - 7(2\xi) + 4] \cos(\omega t) \text{ on } \xi \in [0, 0.5],$$

$$T' = -a \frac{81}{16} (2-2\xi)^3 [3(2-2\xi)^2 - 7(2-2\xi) + 4] \cos(\omega t) \text{ on } \xi \in [0.5, 1], \quad (0.7)$$

is used to generate a harmonic perturbation wave of angular frequency ω and an amplitude determined by the amplitude coefficient a . Here again, the auxiliary coordinate $\xi \in [0, 1]$ is then scaled to the desired heating strip extent $x_{p,0} \leq x \leq x_{p,1}$. A mono-frequential perturbation with $\omega = 0.09$ and $a = 0.75$ was found to trigger rapid transition due to non-linear interactions and was used to obtain the following results.

0.3 Results

All results presented are obtained after all initial transients have died out, i.e. taken from a period on the limit cycle. The following three paragraphs are dedicated to the instantaneous coherent flow structures of the transitional flow structures, the mean flow deformation, and the spectral content of the transient flow field.

Coherent structures of transitional flow Instantaneous isosurfaces of the λ_2 -criterion are depicted in figure 0.3. It can be seen that turbulence develops in form of a turbulent wedge originating from the near-corner region. A closer look at the flow

structures in the initial phase of the transition as depicted in figure 0.3b reveals the emergence of hairpin vortices, typically observed during the transition process, see e.g. [12]. Note that while the perturbation flow field appears symmetric with respect to the corner bisector in the initial stage of the transition process as seen in figure 0.3b, the symmetry is broken further downstream as can be deduced from a closer look at individual flow structures in figure 0.3a. The break of symmetry is likely to stem from small numerical errors and/or the alternating up- and downwind biased compact finite difference scheme used. However, the break of symmetry is an inherent feature of turbulence, and a perturbation-free environment is not experimentally realizable, either.

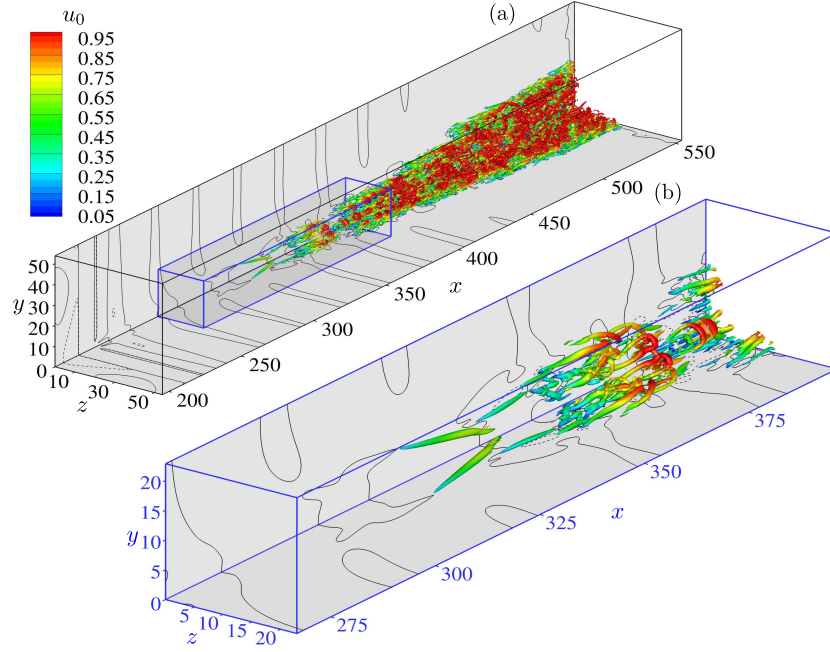


Fig. 0.3 Snapshot visualization of the transition process; isosurfaces of the λ_2 -criterion [6] at $\lambda_2 = -0.01$ colored by the local streamwise velocity of the base state and isocontours of the wall pressure perturbation at $\rho' = 0.002$ (—) and $\rho' = -0.002$ (---): (a) entire computational domain and (b) enlarged view of the DMD subdomain as listed in the top and bottom row of table 0.2, respectively.

Mean flow deformation The time-averaged streamwise velocity $\bar{\mathbf{u}} = N^{-1} \sum_{i=1}^N \mathbf{u}_i$ and mean flow deformation $\bar{\mathbf{u}} - \mathbf{u}_0$ field at the beginning, in the middle, and at the end of the post-processing subdomain are depicted in figure 0.4. By comparing with the laminar base state depicted in figure 0.2a it is observed that the flow field at $x = 267.49$ in figure 0.4a still closely resembles the self-similar solution. The velocity isolines in the domain center in figure 0.4b exhibit a distortion in form of a

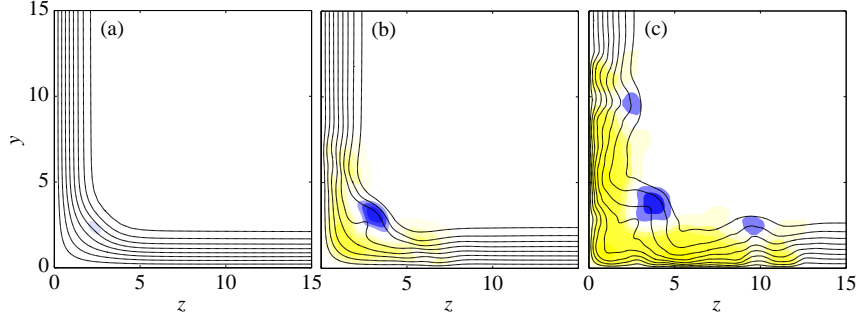


Fig. 0.4 Contours of the time-averaged streamwise velocity (—) and mean flow deformation (filled: (yellow/bright) positive, (blue/dark) negative) in transversal planes at (a) $x = 267.49$, (b) $x = 332.12$, and (c) $x = 396.74$, corresponding to the beginning, the middle, and the end of the DMD subdomain, respectively.

convex bulge as seen in experimental studies [17]. A strong mean flow deformation is observed in figure 0.4c for $x = 396.74$ where an additional outward bulge can be seen at $\eta, \zeta \approx 10$ on each of the walls. The latter correspond to the hairpin vortices flanking the bisectorial centered vortex structure seen in figure 0.3.

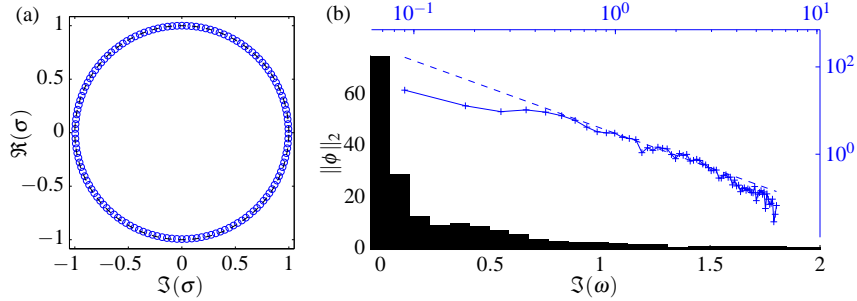


Fig. 0.5 Dynamic mode decomposition from 140 snapshots over one fundamental period; (a) empirical Ritz values (\circ); (b) magnitudes of the Koopman modes on a linear (black bars) and a logarithmic scale (—). The dashed line (---) shows a slope of $\Im(\omega)^{-5/3}$.

Spectral analysis The global stability properties of the transient flow field are best analysed by means of a spectral decomposition technique, i.e. decomposition into global modes of a single frequency. Here, we use the Koopman operator-based dynamic mode decomposition (DMD) introduced by Schmid [15] and analysed in detail by Rowley et. al. [13]. The reader is referred to the latter literature for details on the method. The empirical Ritz values are depicted in figure 0.5a in the complex plane. It can be seen that all Ritz values are located on the unit circle, indicating zero temporal growth as expected for a convective problem on its limit cycle. Also, the values are evenly distributed, meaning that the flow field is clearly

decomposed into mono-frequential modes of integer multiples of the forcing frequency. The modal amplitudes are shown in figure 0.5b as a function of the modal frequency on a linear and a logarithmic scale. The first Koopman mode is found to be the most energetic. This result is not surprising as the first mode embodies the steady component with $\omega = 0$ which is similar but not necessarily equal to the mean flow deformation, cf. Chen et. al. [4]. The second most energetic mode is the direct response of the base state to the forcing frequency at $\omega = 0.09$. For higher frequencies, the modal energy distribution is found in good agreement with the $-5/3$ power-law of the inertial subrange of the energy cascade [7].

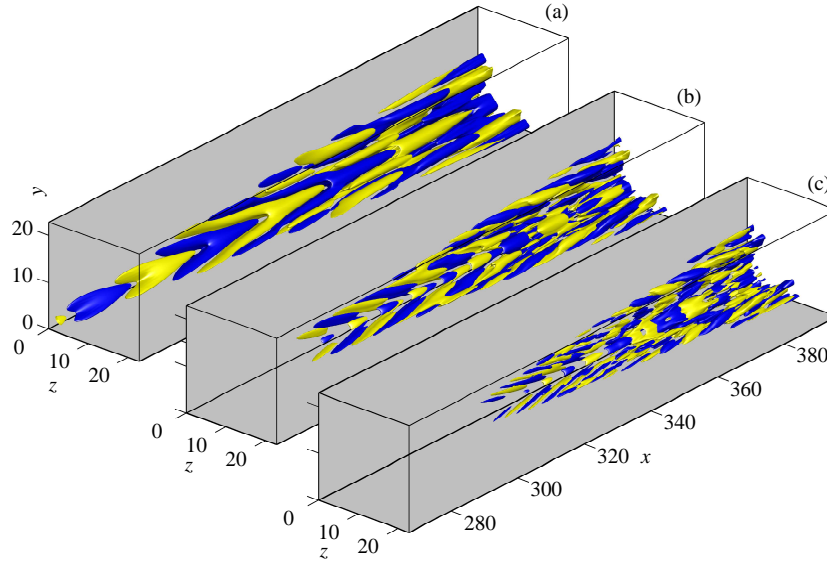


Fig. 0.6 Dynamic modes from the visualized by isosurfaces of the streamwise perturbation velocity: (a) fundamental frequency $\Im(\omega) = 0.09$, (b) first higher harmonic $\Im(\omega) = 0.18$, and (c), second higher harmonic $\Im(\omega) = 0.27$. Isosurfaces are drawn at $\pm 0.2|u'|_{max}$.

The modal structures corresponding to the fundamental frequency and the first two higher harmonics are visualised in figure 0.6. The coherent flow structures appear elongated as commonly observed in non-linearly developing flows. It can also be seen that energy is distributed towards higher wave numbers in accordance with the energy cascade. This is clearly indicated by the increasingly fine flow patterns when comparing the modes in the given order of increasing frequency.

0.4 Performance

Originally the *NS3D* program was designed and optimized for the vector computing architecture of the NEC-SX supercomputers at HLRS Stuttgart. A combination of shared and distributed memory parallelization features are applied to account for the typically small ratio of CPUs per node to overall number of nodes. A sketch of the layout is shown in figure 0.7. The computational domain is decomposed in blocks of equal number of grid points by splitting the streamwise and wall-normal direction. These blocks communicate via MPI routines [9] to exchange neighbouring data. Additionally the spanwise direction is parallelized by means of openMP directives [10]. Details of the algorithm can be found in [1].

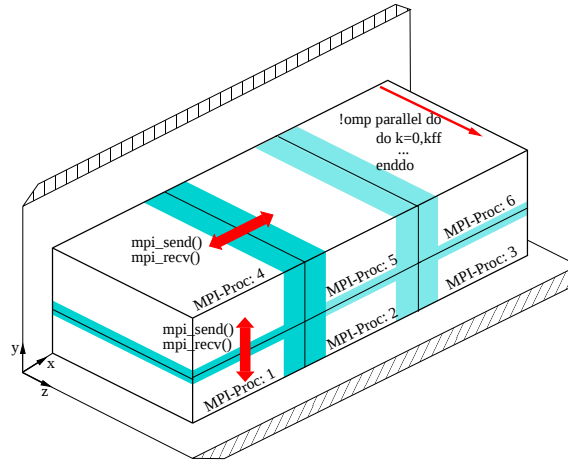


Fig. 0.7 Domain decomposition in x - and y -direction and parallelization features in *NS3D* program

In spanwise direction the classical Thomas algorithm is applied independently on each process in order to efficiently solve the linear system of equations arising from the compact finite difference scheme, i.e. equations 0.4, 0.5, 0.6. In streamwise and wall-normal direction however a pipelined version of the Thomas-algorithm [11] is implemented which fully conserves the order of the compact scheme across domain, i.e. process boundaries along the respective direction. Unfortunately this comes at the expense of idle CPU time for subsequent processes as illustrated in figure 0.8. As long as the number of linear systems is sufficiently larger than the number of processes, which has been the case for the NEC-SX vector computers, the benefit of the homogeneous order throughout the whole domain outdoes the computationally costly idling. On scalar architecture computers on the other hand the ratio of CPUs per node to overall number of nodes usually is less advantageous for a pipelined computation of the linear systems of equations. One has to compensate the reduced specific CPU times encountered on scalar computers by a larger number of processes. For small scale problems the CPU time per grid point and time step (specific CPU time) on vector parallel computers (NEC-SX9) and massively parallel comput-

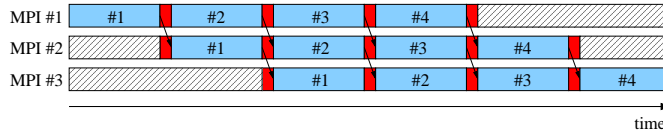


Fig. 0.8 Pipelined Thomas algorithm: blue indicates compute time, hatched indicates idle time. Reproduced from [1]

ers (XE6) are comparable but the NEC SX computers exhibit a large performance boost due to the vectorization for large numbers of grid points as they are usually encountered in direct numerical simulations (cf. table 0.3). Taking into account the expansion in z -direction it was opted to use 200 nodes to distribute a total of $2 \cdot 10^8$ grid points on the Cray XE6 supercomputer to simulate the problem at hand. Each node was set to use 32 threads for openMP parallelized tasks. Additionally

Table 0.3 Comparison of CPU time per grid point and time step.

| Grid | Time steps | Specific CPU time [μ s] | |
|------------|------------|------------------------------|----------|
| | | NEC-SX9 | Cray XE6 |
| 100 x 100 | 10000 | 2.257 | 3.051 |
| 250 x 1000 | 10000 | 0.335 | 3.791 |

20 nodes have been employed to perform online postprocessing routines. Two runs of 22 hrs each where necessary to reach the limit cycle at which the sampling for all subsequent analysis was undertaken. The specific CPU time for these computations amounted to excruciatingly high 56μ s per grid point and timestep stemming foremost from the use of a pipelined linear systems solver. Figure 0.9 underlines

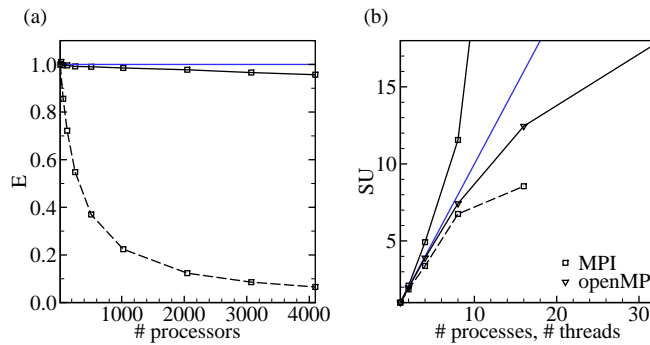


Fig. 0.9 Parallel scaling of compact FD (dashed line) and subdomain compact FD (solid line) scheme. (a) Efficiency (weak scaling); (b) Speedup (strong scaling) for openMP and MPI parallelization. Ideal efficiency and speedup are indicated by blue lines

the massive performance drop of the MPI parallelization in combination with the coupled linear systems on the XE6. The efficiency E is obtained from weak scaling tests on a range of 1-256 MPI processes using 16 CPUs each. Using 4 processes already leads to only 50% efficiency which keeps on dropping down to 7% for the largest simulation. Strong scaling tests underline the suboptimal parallelization of the pipelined Thomas algorithm on a scalar computer. The speedup, defined as ratio of sequential compute time to parallel compute time $SU = T_1/T_P$, depicts strong sublinear behaviour starting from 8 processes and onwards. For the sake of completeness the speedup for purely openMP parallelized stimulations is also shown in figure 0.9. Almost ideal speedup can be reached for up to 8 threads which correlates to the size of a NUMA node within a compute node of the Cray XE6 computer. For 9-32 threads still sufficient albeit slightly sublinear speedup can be obtained. In order to significantly improve the parallelization for future simulations a so-called sub-domain compact scheme has been implemented into the *NS3D* program. This scheme decouples the discretization in x - and y -direction such that the linear system of equations can be solved independently on each sub-domain. For that purpose it is necessary to partly replace the left hand side of the compact stencil at domain boundary points by explicit values. In order to sustain the characteristic wave resolution of the compact scheme explicit finite differences of 8th order are used to compute these values. Performing the aforementioned scaling analysis for the new solver routine demonstrates the near-ideal efficiency reached by decoupling the domains as well as a superlinear speedup due to favourable cache effects for the regarded problem size.

0.5 Conclusions

A direct numerical simulation of the transition in streamwise corner-flow at a technically relevant Mach number of $Ma = 0.8$ was conducted. The transition takes place in form of a turbulent wedge situated in the near-corner region. This result is remarkable in the sense that it is found in accordance with measurements but in opposition to linear theory which does not predict a dominant instability mechanism due to the presence of the corner as compared to the single flat-plate scenario. The turbulent flow structures were found in agreement with other wall-bounded shear flows, and the spectral content of the transitional flow extracted via direct mode decomposition of a snapshot sequence was found to match the theoretically predicted power-law. From the computational side, the DNS code was found to perform inferior in the massive parallel environment of the CRAY XE6 as compared to the vector architectures it was originally designed for. However, a recently developed recast sub-domain compact scheme allowed for a decoupled processing of the routines while maintaining the overall accuracy of its fully implicit precursor. The decoupling led to a significant gain in computational performance for distributed memory parallelization. Scaling tests indicated almost ideal efficiency and superlinear speedup

for the new implementation. Scaling tests for the shared memory parallelization showed almost ideal speedup for up to 8 threads as well.

References

1. Babucke, A.: Direct numerical simulation of noise-generation mechanisms in the mixing layer of a jet. Ph.D. thesis, Universität Stuttgart (2009)
2. Babucke, A., Kloker, M., Rist, U.: DNS of a plane mixing layer for the investigation of sound generation mechanisms. *Computers & Fluids* **37**(4), 360–368 (2008)
3. Carrier, G.: The boundary layer in a corner. *Quarterly of Applied Math* **4**, 367–370 (1947)
4. Chen, K., Tu, J., Rowley, C.: Variants of dynamic mode decomposition: boundary condition, Koopman, and Fourier Analyses. *Journal of Nonlinear Science* pp. 1–29 (2011)
5. Galionis, I., Hall, P.: Spatial stability of the incompressible corner flow. *Theoretical and Computational Fluid Dynamics* **19**, 77–113 (2005). DOI 10.1007/s00162-004-0153-1
6. Jeong, J., Hussain, F.: On the identification of a vortex. *Journal of Fluid Mechanics* **285**(69), 69–94 (1995)
7. Kolmogorov, A.: Dissipation of energy in locally isotropic turbulence **32**(1), 15–17 (1941)
8. Mikhail, A.G., Ghia, K.N.: Viscous Compressible Flow in the Boundary Region of an Axial Corner. *AIAA Journal* **16**, 931–939 (1978). DOI 10.2514/3.60987
9. N.N.: MPI - A message-passing interface standard. Technical Report CS-94-230, University of Tennessee, Knoxville (1994)
10. OpenMP: The openmp api specification for parallel programming (2012). URL <http://www.openmp.org>
11. Povitsky, A.: Parallelization of the pipelined Thomas algorithm. ICASE Report 98-48 (1998)
12. Rist, U., Fasel, H.: Direct numerical simulation of controlled transition in a flat-plate boundary layer. *Journal of Fluid Mechanics* **298**, 211–248 (1995)
13. Rowley, C., Mezić, I., Bagheri, S., Schlatter, P., Henningson, D.: Spectral analysis of nonlinear flows. *Journal of Fluid Mechanics* **641**(1), 115–127 (2009)
14. Rubin, S.G., Grossman, B.: Viscous flow along a corner: numerical solution of the corner layer equations. *Quarterly of Applied Mathematics* **29**, 169–186 (1971)
15. Schmid, P.J.: Dynamic mode decomposition of numerical and experimental data. *Journal of Fluid Mechanics* **656**, 5–28 (2010). DOI 10.1017/S0022112010001217
16. Schmidt, O., Rist, U.: Linear stability of compressible flow in a streamwise corner. *Journal of Fluid Mechanics* **688**, 569–590 (2011)
17. Zamir, M.: Similarity and stability of the laminar boundary layer in a streamwise corner. *Royal Society of London Proceedings Series A* **377**, 269–288 (1981)